1   **Functionality-Based Formation of Secondary Organic Aerosol from *m*-Xylene**

2   **Photooxidation**

3   Yixin Li[1,2], Jiayun Zhao[1], Mario Gomez-Hernandez[1], Michael Lavallee[3], Natalie H. Johnson[4],

4   and Renyi Zhang[1,3*]

5   [1]Department of Chemistry, Texas A&M University, College Station, TX 77843, USA

6   [2]Department of Chemistry, University of California Irvine, Irvine, CA 92697, USA

7   [3]Department of Atmospheric Sciences, Texas A&M University, College Station, TX 77843,

8   USA

9   [4]Department of Environmental & Occupational Health, School of Public Health, Texas A&M

10   University, College Station, TX 77843, USA

11

12   **ABSTRACT**. Photooxidation of volatile organic compounds (VOCs) produces condensable

13   oxidized organics (COOs) to yield secondary organic aerosol (SOA), but the fundamental chemical

14   mechanism for gas-to-particle conversion remains uncertain. Here we elucidate the production of

15   COOs and their roles in SOA and brown carbon (BrC) formation from *m*-xylene oxidation by

16   simultaneous monitoring the evolutions of gas-phase products and aerosol properties in an

17   environmental chamber. Four COO types with the distinct functionalities of dicarbonyls,

18   carboxylic acids, polyhydroxy aromatics/quinones, and nitrophenols are identified from early-

19   generation oxidation, with the yields of 25%, 37%, 5%, and 3%, respectively. SOA formation

20   occurs via several heterogeneous processes, including interfacial interaction, ionic

21   dissociation/acid-base reaction, and oligomerization, with the yields of $(20 \pm 4)\%$ and $(32 \pm 7)\%$

22   at 10% and 70% relative humidity (RH), respectively. Chemical speciation shows the dominant

23   presence of oligomers, nitrogen-containing organics, and carboxylates at high RH and

24   carboxylates at low RH. The identified BrC includes N-heterocycles/N-heterochains and

25   nitrophenols, as evident from reduced single scattering albedo. The measured uptake coefficient

26   (γ) for COOs is dependent on the functionality, ranging from 3.7×10^{-4} to 1.3×10^{-2}. A kinetic

27   framework is developed to predict SOA production from the concentrations and uptake

28   coefficients for COOs, and this functionality-based approach well reproduces SOA formation from

                                                        1

29   *m*-xylene oxidation. Our results reveal that photochemical oxidation of *m*-xylene represents a

30   major source for SOA and BrC formation under urban environments, because of its large

31   abundance, high reactivity with OH, and high yields for COOs.

32   **Corresponding to:** Email: renyi-zhang@tamu.edu

33

34   **1.   Introduction**

35   Photooxidation of anthropogenic and biogenic volatile organic compounds (VOCs)

36   produces tropospheric ozone, secondary organic aerosol (SOA), and brown carbon (BrC), with

37   profound implications for air quality, human health, and climate (Pope et al., 2002; Li et al., 2007;

38   IPCC, 2013; NASEM, 2016; Molina, 2021; Zhang et al., 2021). For example, SOA contributes to

39   the Earth energy budget, directly by scattering solar radiation and indirectly by serving as cloud

40   condensation nuclei to influence cloud formation and precipitation (IPCC, 2013; Wang et al., 2014;

41   Zhu et al., 2017). Also, light absorbing BrC interferes with solar radiation transfer, contributing to

42   positive radiative forcing (Wang et al. 2013; NASEM, 2016). VOC oxidation is initiated by various

43   oxidants (e.g., OH, O_3, NO_3, etc.) and proceeds via multiple pathways and stages (Atkinson, 2000;

44   Suh et al., 2001; Zhang et al., 2002; Zhao et al., 2004; Wennberg et al., 2018), yielding condensable

45   oxidized organics (COOs) to form SOA and BrC via gas-to-particle conversion (Finlayson-Pitts

46   and Pitts, 2000; Moise et al., 2015; Seinfeld and Pandis, 2016). Currently, the enormous chemical

47   complexity for VOC oxidation and gas-to-particle conversion represents one of the greatest

48   challenges in atmospheric chemistry research (Ravishankara, 1997; Zhang et al., 2015; NASEM,

49   2016). Aromatic hydrocarbons (e.g., benzene, toluene, xylenes, and trimethylbenzene) account for

50   20-30% of the total VOCs and are the major anthropogenic SOA precursors in the urban

51   atmosphere (Calvert et al., 2002; Ng et al., 2007; Song et al., 2007; Guo et al., 2014; Seinfeld and

52   Pandis, 2016). For example, *m*-xylene or $C_6H_4(CH_3)_2$ represents an important type of aromatic

53   hydrocarbons, which is emitted primarily from industrial and traffic sources. The concentration of

2

54   *m*-xylene ranges in a level from sub part per billion (ppb) up to several tens of ppb under urban

55   environments (Calvert et al., 2002; Fortner et al., 2009). Photooxidation of *m*-xylene is primarily

56   initiated by OH with a rate constant of 2.4×10^{-11} cm^3 molecule^{-1} s^{-1}, which is nearly four times

57   higher than that of toluene (Fan and Zhang, 2008; Ji et al., 2017). A laboratory study identified *m*-

58   tolualdehyde, *m*-dimethylphenols, and dicarbonyls (i.e., glyoxal, methylglyoxal, unsaturated

59   dicarbonyls, and epoxy carbonyls) as the main gas-phase products from OH-initiated oxidation of

60   *m*-xylene (Zhao et al., 2005).

61   Several types of condensable oxidized organics (COOs) with distinct functionality and

62   volatility are produced form *m*-xylene photooxidation, contributing to aerosol nucleation and grow

63   (Zhang et al., 2004; Zhang et al., 2015; Guo et al., 2020). SOA formation is conventionally

64   considered to be mainly resulted from equilibrium gas-particle partitioning of semi-, intermediate-,

65   or low-volatile products (Shrivastava et al., 2017). Aromatic oxidation by OH yields low-volatile

66   polyhydroxy aromatics/quinones (denoted as PAQ hereafter), which condense to the aerosol-phase

67   (Schwantes et al., 2017). Also, chain autoxidation reactions of RO$_2$ from aromatics photooxidation

68   likely yield highly oxygenated molecules (HOMs) with low volatility (Molteni et al., 2018;

69   Garmash et al., 2020; Wang et al., 2020), although the reported yield of HOMs from *m*-xylene

70   oxidation is small (1.0-1.7%) (Molteni et al., 2018). Several key oxidation products of aromatic

71   oxidation have been shown to readily engage in multiphase reactions and contribute to SOA

72   formation (Ji et al., 2020, Li et al., 2021a). A recent experimental study demonstrated that SOA

73   formation from toluene photooxidation is mainly contributed by volatile dicarbonyls and organic

74   acids (Li et al., 2021b). Moreover, the aqueous reactions between small α-dicarbonyls and base

75   species (e.g., ammonia and amines) produce light-absorbing brown carbon (BrC) (De Haan et al.,

76   2011, 2017; Marrero-Ortiz et al., 2019; Li et al., 2021a,b). Previous experimental studies identified

77 the presence of hydroxy (C-OH), carbonyl (C=O), and acetal (C-O-C) functional groups in

78 aromatic-derived SOA formed via aqueous reactions, implicating a role of oxygenated organics in

79 SOA formation (Jia and Xu, 2014; Jia and Xu, 2018; Zhang et al., 2019). Also, laboratory

80 experiments showed that coating of *m*-xylene SOA on black carbon particles significantly

81 enhances scattering, absorption, and single scattering albedo (SSA) (Guo et al., 2016).

82   Current atmospheric models mainly parameterize SOA formation based on equilibrium

83 partitioning for semi- to low-volatile COOs (Shrivastava et al., 2017). However, gas-to-particle

84 conversion corresponds to decreasing entropy (i.e., $\Delta S \ll 0$), represents non-equilibrium chemical

85 processes (Peng et al., 2021). Moreover, the occurrence of particle-phase reactions significantly

86 alters the physiochemical properties (including volatility, hygroscopicity, and optical properties)

87 for COOs (Tan et al., 2012; Faust et al., 2017; Ji et al., 2020; Li et al., 2021a,b; Liu et al., 2021).

88 Notably, the volatility-based approach consistently under-predicts SOA formation (Heald et al.,

89 2005; Zhang et al., 2015; Hodzic et al., 2016), particularly during haze formation under polluted

90 conditions (Guo et al., 2014; Peng et al., 2021). Here we investigate the production of COOs with

91 different functionalities and assess their roles in SOA formation from *m*-xylene oxidation. A

92 primary objective of this work is to establish a functionality-based framework to predict SOA

93 formation from VOC photooxidation.

94 **2.   Experimental Methodology**

95 **2.1   Chamber experiments**

96   The production of COOs and their roles in SOA formation from *m*-xylene oxidation were

97 investigated using a 1 m^3 chamber (Teflon® PFA, Fig. S1 in the Supplementary Information or

98 SI), similar to our previous studies (Li et al., 2021a,b). The environmental chamber was equipped

99 with eighteen black light lamps (18 × 30W, F30T8/350BL, Sylvania). A water bubbler at a

100 temperature of 30°C was used to humidify the chamber to 10%, 30%, 50%, or 70% relative

101 humidity (RH), and all experiments were performed at 298 K. Three types of seed particles were

102 produced using a constant output atomizer (Model 3076, TSI) to represent various chemical

103 compositions, i.e., NH_4HSO_4 - ammonium bisulfate (ABS), $(NH_4)_2SO_4$ - ammonium sulfate (AS)

104 in the presence and absence of NH_3, and NaCl - sodium chloride. Seed particles were dried to RH

105 of ~2% by a Nafion drier (PD-070−18T-12SS, Perma Pure) and size-selected for an initial size of

106 100 nm by a differential mobility analyzer (DMA, Model 3081, TSI). Size-selected particles were

107 injected into the chamber with an initial particle concentration of 1.5×10^4 cm^{-3} measured by a

108 condensation particle counter (CPC, Model 3760A, TSI). The acidity of seed particles was

109 estimated using a thermodynamic model (Fountoukis and Nenes, 2007; Wang et al., 2018), with

110 the pH value of 3~5 in the presence of gaseous NH_3 and 0~1 in the absence of gaseous NH_3 for

111 $(NH_4)_2SO_4$, -0.5 for NH_4HSO_4, and 7 for NaCl. To investigate the effects of NH_3 and NO_x,

112 commercially available gaseous NH_3 (2000 ppm NH_3 in N_2) and NO_2 (500 ppm NO_2 in air) was

113 injected into the chamber with a flow of 100 sccm. 600 μL H_2O_2 (35 wt%, Sigma-Aldrich) and 10

114 μL m-xylene (99.5%, Sigma-Aldrich) were injected into a glass reservoir, which was then flushed

115 into the chamber by a 10 slpm flow from a pure air generator (Aadco 737-11, Aadco Inc.) for 10

116 min. The gases were then mixed by a fan inside the chamber. Once desired concentrations were

117 established, the black light lamps were turned on to initiate H_2O_2 photolysis to generate OH

118 radicals. The initial concentration for m-xylene and the steady-state concentration for OH were

119 estimated to be 1.9 ppm and 2.1×10^6 molecules cm^{-3}, respectively (Fig. 1a). The experimental

120 conditions are summarized in Table 1.

121 **2.2   Analytical instruments**

122   The particle size growth, density, light scattering/absorption were simultaneously and

123   continuously monitored, after monodispersed seed particles were exposed to the products of *m*-

124   xylene-OH oxidation in the reaction chamber. A scanning mobility particle sizer (SMPS)

125   consisting of a DMA and a CPC was used to continuously measure the particle size growth factor,

126   GF = D_p/D_0, where D_p is the diameter after exposure and D_o = 100 nm is the initial diameter. Note

127   both D_p and D_0 correspond to the dry particle diameter measured after passing through a Nafion

128   dryer (~2% RH). An aerosol particle mass analyzer (APM, Model 3600, Kanomax) was used to

129   derive the particle density throughout the experiments (Li et al., 2021b). The density for the SOA

130   materials (ρ_{SOA}) is calculated by,

$$\rho_{SOA} = \frac{\rho \times GF^3 - \rho_0}{GF^3 - 1} \qquad (1)$$

131   where ρ and GF are measured particle density (g cm^{-3}) and growth factor at *t* (min), respectively.

132   ρ_0 is the initial density of seed particles. The uncertainty in the density measurements was

133   estimated to be $\pm$ 0.03 g cm^{-3}.

134   To measure the optical properties of exposed particles, a 1-slpm flow from the chamber

135   was diluted by 4-slpm N$_2$ and introduced into a commercial integrating nephelometer (TSI 3563)

136   and a home-built cavity ring-down spectrometer (CRDS) throughout the experiment. Light

137   scattering (b_{sca}) and extinction (b_{ext}) at 532 nm were determined by the nephelometer and CRDS,

138   respectively. The nephelometer was calibrated by comparing measured b_{sca} with b_{ext} from CRDS

139   when measuring ammonium sulfate particles with diameters of 100 nm, 150 nm, 200 nm, 250 nm,

140   and 300 nm. The absorption coefficient (b_{abs}) was determined from ($b_{ext} - b_{sca}$), and SSA was

141   calculated from b_{sca}/b_{ext}.

142   The ID-CIMS using the hydronium reagent ion (H$_3$O$^+$) was employed to analyze gaseous

143   concentrations with a sample flow rate of 0.5 slpm from the chamber. The sample line was heated

144   to 70°C to reduce wall loss. Gas-phase concentrations of m-xylene and its oxidation products were

145   quantified by ID-CIMS. Briefly, the concentration of species A from the proton transfer reaction

146   ($H_3O^+ + A \rightarrow H_2O + HA^+$) is determined by,

$$[A] = \frac{S_A}{k_{PTR} \times \Delta t \times S_{RI}} \tag{2}$$

147   where S_A and S_{RI} are the mass spectrum intensities for A and reagent ions, respectively. k_{PTR} is the

148   proton-transfer rate constant between A and H_3O^+ (Zhao and Zhang, 2004). $\Delta t = \frac{l}{U_i}$ is the retention

149   time of ions, which is determined by the length of the drift tube $l = 8$ cm and the ion drift velocity

150   U_i. The ion drift velocity U_i is determined from:

$$U_i = u_0 (\frac{760 \ torr}{p})(\frac{T}{273 \ K})E \tag{3}$$

151   where $u_0 = 2$ cm^2 V^{-1} s^{-1} is the reduced ionic mobility (Dotan et al., 1976), $p = 3.0$ torr, $T = 298$ K,

152   and $E = 133$ V cm^{-1} is the voltage gradient in the drift tube. Alternatively, the concentrations of m-

153   xylene, dicarbonyls, and organic acids were also calibrated by preparing the vapors of m-xylene,

154   methylglyoxal with known mixing ratios in N_2, and using a permeation tube of propanoic acid,

155   respectively (Li et al., 2021a). The detection limit (defined as 3 times of the ratio of signal to noise)

156   for the oxidation products from m-xylene-OH reactions was estimated to be 50 ppt by the ID-

157   CIMS.

158   The steady-state OH concentration was determined by exponential fitting ($y = ke^{-bx}$) of

159   the decay of m-xylene concentration (Fig. 1a),

$$[OH] = \frac{b}{k_1} \tag{4}$$

160   where $k_1 = 2.4 \times 10^{-11}$ cm^3 molecule^{-1} s^{-1} is the second-order rate constant for *m*-xylene-OH

161   oxidation (Fan and Zhang, 2008). The estimated concentration of OH was 2.1×10^6 molecules cm^{-3}

162   in our experiments.

163   We also estimated loss of condensable vapors to the chamber wall using the first-order

164   wall-loss coefficient, kw (s^{-1}), by considering gas-phase transport within the chamber (Zhang et

165   al., 2014)

$$kw = (\frac{A}{V}) \frac{\alpha_w \bar{c}}{4 + \frac{\pi}{2}\left(\frac{\alpha_w \bar{c}}{\sqrt{k_e D_g}}\right)} \tag{5}$$

166   where A/V is the surface to volume ratio of the chamber (equal to 6/L for a square chamber, where

167     $L = 1$ m is its dimension), α_w is the mass accommodation coefficient of vapors onto Teflon chamber

168   walls, $\bar{c}$ is the mean thermal speed of the molecules, k_e is the coefficient of eddy diffusion, which

169   is estimated to be 0.5 based on the loss rate of particles (McMurry and Rader, 1985),

$$k_e = \frac{(\frac{\pi L \beta_0}{12})^2}{D_b} \tag{6}$$

170   where β_0 is the fractional loss rate of particles,

$$\beta_0 = \frac{\Delta N}{N \times \Delta t} = \frac{15000 \text{ cm}^{-3} - 7500 \text{ cm}^{-3}}{15000 \text{ cm}^{-3} \times 7200 \text{ s}} = 1.4 \times 10^{-5} \text{ s}^{-1} \tag{7}$$

171   where N is the particle number concentration, $D_b = 6.75 \times 10^{-10}$ m^2 s^{-1} is the Brownian diffusion

172   coefficient for particles. D_g is the gas-phase diffusion coefficient. For NH$_3$, the mass

173   accommodation coefficient of vapors onto the chamber wall is 0.05 (Zhang et al., 2014). Gas-

174   phase diffusion constant D_g is 1.98×10^{-5} m^2 s^{-1}. The mean thermal speed $\bar{c}$ is 603 m s^{-1}. The first-

175   order wall-loss coefficient of NH$_3$ was calculated to be 1.2×10^{-2} s^{-1}.

176   The average concentration of NH$_3$ or NO$_x$ (noted as X) is estimated by,

$$\overline{[X]} = \frac{(1 - e^{-k_w \times \Delta t_i})}{k_w \times \Delta t_i} [X]_0 \qquad (8)$$

177   For initial injection of 400 ppb NH_3, the average concentration of NH_3 was estimated to be 19 ppb.

178   The first-order wall-loss rate of NO_x was measured to be $2.5 \times 10^{-3}\,h^{-1}$, leading to negligible wall-

179   loss (Qi et al., 2020).

180   The particle-phase chemical composition was analyzed by thermal desorption (TD) - ID -

181   CIMS (TD-ID-CIMS) (Wang et al., 2010). Seed particles after 20 min of exposure to

182   photooxidation were collected for 2 hours by a platinum filament (with a collection voltage of

183   about 3000 V) in a 2.5 slpm flow from the reaction chamber, and the analytes were evaporated by

184   heating the filament to 350^oC for 2 s and detected by ID-CIMS using H_3O^+ as the reagent ions.

185   The mass resolution of TD-ID-CIMS was about 0.5 amu. The desorption signal was represented

186   by the relative intensity (RI) of the integrated peak area during heating. The uncertainties of TD-

187   ID-CIMS measurements arose from the flow rate, voltage, collection time, evaporation voltage,

188   and mass spectrometer ionization/detection efficiencies during particle collection and were

189   represented by the standard deviation of three repeated measurements. In both ID-CIMS and TD-

190   ID-CIMS configurations, an ion drift- tube was used. An electric field of E/N = 138 Td was applied

191   for ID-CIMS at high RH (i.e., 70%), and E/N = 110 Td was used for TD-ID-CIMS at low RH (<

192   1%). Formation of cluster ions was effectively suppressed, since a uniform electrical field in the

193   drift tube decomposed weakly-bonded cluster ions. Fragmentation using ID-CIMS or TD-ID-

194   CIMS was minimal, and all gaseous and particle-phase products were detected at their respective

195   parent-peaks, indicating little dissociation effect from either thermal desorption or ionization by

196   H_3O^+(Yuan et al., 2017). For example, the major molecules detected by TD-ID-CIMS at high RH

197   from *m*-xylene oxidation were acetal/hemiacetal oligomers, consistent with a previous study

198   showing intact oligomers with thermal desorption (Claflin and Ziemann, 2019).

199　　　　While the gaseous concentrations of the oxidation products, GF, SSA, and density were

200　temporally resolved in our experiments, the particle chemical composition reflected an overall

201　aerosol chemical makeup during an experiment. To assess the effects of different seed particles,

202　RH, and NH$_3$ on SOA and BrC formation, we compared the measured GF and SSA values after

203　120-min exposure to the *m*-xylene-OH oxidation.

2.3 Uptake coefficient (γ) determination

205　　　　The uptake coefficient (γ) for COOs is calculated by,

$$\gamma = \frac{4 \times FR \times kp}{\bar{c} \times S} \tag{9}$$

206　where FR is the percent contributions of the COO species from *m*-xylene-OH oxidation to the

207　particle-phase mass intensity measured by TD-ID-CIMS. kp is measured first-order particle uptake

208　rate constant for COOs (i.e., glyoxal, methylglyoxal, γ-dicarbonyls, organic acids, PAQ, and

209　nitrophenols), which is calculated from the measured growth rate of seed particles,

$$kp = \frac{\pi \times \left(D_p^3 - D_0^3\right) \times \rho \times \bar{N} \times N_A}{6 \times MW \times [A] \times \Delta t} \tag{10}$$

210　where D_p and D_0 are the final and initial diameters of the particles during the time-period of,

211　respectively, ρ is the density of total SOA, $\bar{N}$ = 11250 cm^{-3} is the average particle number

212　concentration during 120 min, Δt = 120 min is the exposure time, N_A is Avogadro constant, MW

213　is the molar weight of species A, and [A] is the average gas phase concentration of species A. $\bar{c}$ is

214　the mean thermal speed of A. S is the average surface area of aerosols (cm^2 surface/cm^3 air) during

215　the period of Δt = 120 min,

$$S = \frac{\pi \int_{t=0}^{120 \text{ min}} D^2 \times HGf^2 \times \bar{N} dt}{\Delta t} \tag{11}$$

216   where D is the time-dependent particle diameter, HGf is the hygroscopic growth factor of particles

217   (Seinfeld and Pandis, 2016). The error bars of reactive coefficients are derived from the

218   propagation of uncertainties for the parameters in eqs. 9-11 (i.e., 1 σ of at least three repeated

219   measurements for each parameter).

2.4   Simulation of gaseous oxidation products

221   The gas-phase concentration of m-xylene-OH oxidation products were simulated by a tri-

222   exponential kinetic model to account for the gas-phase oxidation, chamber wall loss, and particle

223   uptake. The precursor A with an initial concentration of $[A]_0$ undergoes multiple steps of oxidation

224   to yield multi-generation products, P_n (where $n = 1, 2, 3, \ldots$). Once formed, each product engages

225   in further oxidation with a pseudo first-order rate constant of $k_{n+1}' = k_{n+1}[OH]_{ss}$, particle uptake

226   with a rate of kp_n, and wall loss with a rate of kw_n. The forward rate constants, k_{n+1}, were taken

227   from MCM 3.3.1 (Jenkin et al., 2003). The rate of uptake kp_n is expressed by,

$$kp_n = \frac{1}{4}\gamma_n \bar{c} S \qquad (12)$$

228   and the first-order wall loss rate constants were estimated by eq. 5 with the mass accommodation

229   coefficients α_w constrained by the measured time-dependent concentration. The gas-phase

230   concentrations of P_1 to P_3 are calculated by,

$$[P_1] = \frac{k_1'[A]_0}{k_2' + kw_1 + kp_1 - k_1'}(e^{-k_1't} - e^{-(k_2'+kw_1+kp_1)t}) \qquad (13)$$

$$[P_2] = C_1 e^{-(k_3'+kw_2+kp_2)t} + C_2 e^{-k_1't} - C_3 e^{-(k_2'+kw_1+kp_1)t} \qquad (14)$$

$$[P_3] = C_4 e^{-(k_4'+kw_3+kp_3)t} + C_5 e^{-(k_3'+kw_2+kp_2)t}$$
$$+ C_6 e^{-k_1't} - C_7 e^{-(k_2'+kw_1+kp_1)t} \qquad (15)$$

231   where C_1 to C_7 are constants, and k'_n denotes the pseudo-first order rate constant,

$$k'_n = k_n[OH] \qquad (16)$$

232   The rate constants and values for C_1 to C_7 are summarized in Table S1.

2.5   COO yield

The COO yield (Y_{COO}) from *m*-xylene oxidation is determined from,

$$Y_{COO} = [COO_i]/\Delta[C_6H_4(CH_3)_2] \tag{17}$$

where *i* represents the type of COO species, and $\Delta[C_6H_4(CH_3)_2]$ denotes the concentration of *m*-xylene consumed due to OH oxidation. There were four types of COOs identified from our experiments, i.e., dicarbonyls for $i = 1$, carboxylic acids for $i = 2$, PAQ for $i = 3$, and nitrophenols for $i = 4$. The measured gaseous concentration for each COO is corrected for wall-loss and unreacted earlier generation products,

$$[COO_i] = \{[COO_{i,f}] + (\frac{1}{4}\gamma_i \bar{c}S + kw_i)\overline{[COO_i]}\Delta t\}/(1 - \frac{[A_f]}{[A_t]}) \tag{18}$$

where $[COO_{i,f}]$ and $\overline{[COO_i]}$ are the final and time-averaged gas-phase concentrations of COO_i at 120 min, respectively. $[A_f]$ and $[A_t]$ are the unreacted and the total production of the earlier generation species A, respectively.

2.6   SOA mass concentration and yield

The measured SOA mass concentration is calculated based on the aerosol size growth and density,

$$M_{SOA,meas.} = \frac{1}{6}\pi(D_p^3 \times \rho_t - D_0^3 \times \rho_0) \times \bar{N} \tag{19}$$

where ρ_t and ρ_0 are the final and initial particle density during 120 min, respectively. Alternatively, by categorizing COOs in accordance with the functional groups, we established a framework to predict SOA formation from the measured production and reactivity. The SOA mass concentration (M_{SOA}) is predicted from the measured uptake coefficients and average gas-phase concentrations of COOs,

$$M_{\text{SOA}} = \sum_i^4 \frac{1}{4}\gamma_i \bar{c}_i S[A_i]MW_i \qquad (20)$$

252   where MW_i is the molar weight of species i. γ_i is averaged over all identified species for each type

253   (i) of COOs, and $[A_i]$ is the sum of the measured concentrations of all identified species for type i

254   (time-averaged). The SOA mass yield is expressed by,

255    $$Y_{SOA} = M_{SOA}/\{\Delta[C_6H_4(CH_3)_2] \times MW_m\} \qquad (21)$$

256   where MW_m is the molar weight of m-xylene.

257   To compare the measured and predicted SOA formation at RH = 10% and 70%, we

258   corrected the increased vapor wall loss and reduced particle surface area at RH = 70% compared

259   to 10% RH. A correction factor is determined from the average measured gas concentration ratios

260   (R_c) between 10% and 70% RH for each type of COOs. Additionally, a hygroscopic volume

261   enhancement factor (HVE) of 1.2 between 10% and 70% RH is adopted. The RH-corrected SOA

262   mass for each COO is estimated by,

$$M_{i,corr} = R_c \times M_{SOA} \times \frac{S_1}{S_2} \times \text{HVE} \qquad (22)$$

263   where S_1 and S_2 are the particle surface areas at 10% and 70% RH, respectively.

264   **3.   Results and Discussions**

265   **3.1   Evolution of oxidation products**

266   To elucidate the production of COOs, we measured time-dependent gaseous concentrations

267   of m-xylene oxidation products. The OH-m-xylene reactions occur via dominantly OH-addition to

268   the aromatic ring to yield m-xylene-OH adducts and minorly H-abstraction from the methyl group

269   to form methylbenzyl radicals (about 4%) (Fan and Zhang, 2008). The m-xylene-OH adducts then

270   react with O_2 to form dimethylphenol via H-extraction or OH-m-xylene-O_2 peroxy radicals (RO_2)

271   via O_2 addition (Fig. S2a). While the m-xylene mixing ratio exhibits an exponential decay

13

272   throughout the experiments (Fig. 1a), the formation of the gas-phase oxidation products follows

273   the rate-determining steps involving successive OH-oxidation with three major generations (Fig.

274   1b-e). The first-generation products (P_1) include dimeththylphenol (m/z = 123) and

275   methylbenzaldehyde (m/z = 121), corresponding to OH addition to the aromatic ring (~96%) and

276   hydrogen extraction (~4%) from the methyl group, respectively (Fan and Zhang, 2008; Li et al.,

277   2021b). The second-generation products (P_2) mainly consist of methylglyoxal (m/z = 73),

278   methylbutenedial (m/z = 99), toluic acid (m/z = 137), and dimethylresorcinol (Fig. 1f and Fig. S2b),

279   which are produced from the P_1 reactions with OH/HO$_2$. For example, methylglyoxal and

280   methylbutenedial are formed from OH oxidation of dimeththylphenol and subsequent ring-

281   opening or from the primary peroxy radical. The latter undergoes cyclization to form the bicyclic

282   radical, which then reacts with O$_2$ to form the secondary peroxy radical, followed by reactions

283   with HO$_2$ and subsequent ring-cleavage (Fan and Zhang, 2008). The third-generation products (P_3)

284   contain mainly multi-functional organic acids, including pyruvic acid (m/z = 89), 4-oxo-2-

285   pentenoic acid (m/z = 115), and 3-methyl-4-oxo-2-pentenoic acid (m/z = 129) produced from the

286   subsequent reactions of dicarbonyls with OH. Note that P_n in Fig. 1b denotes the lumped product

287   of the nth generation, which is related the sequence of OH addition for m-xylene oxidation and

288   accounts for the various species detected by ID-CIMS (Fig. S2b).

289   The P_1 concentrations rise immediately upon initiating photooxidation and reach the peak

290   mixing ratios of about 20 ppb for dimeththylphenol and 9 ppb for methylbenzaldehyde. There is a

291   slight decline in P_1 concentrations after 70 to 100 mins, reflecting their consumption from further

292   OH oxidation (Fig. 1c). The P_2 concentrations follow those of P_1 (Fig. 1d and Fig. S3a) and reach

293   the peak mixing ratios ranging from 0.4 to 2.4 ppb, dependent on their subsequent oxidation by

294   OH as well as loss to the chamber wall and aerosols. Note that the concentration of toluic acid

295 rises later than those of the dicarbonyls, attributable to the slower rates for H-abstraction by OH

296 from the methyl group than OH-addition to the aromatic ring (Fan and Zhang, 2008). The P_3

297 concentrations increase monotonically after a delay of 10-20 mins and reach a mixing ratio from

298 sub-ppb to 2.5 ppb at 120 min (Fig. 1e and Fig. S3b). The initial concentration of m-xylene (e.g.,

299 1940 ppb) in our experiment is higher than that in the atmosphere, potentially inducing self- and

300 cross-reactions of RO_2 to form alkoxy radicals (RO) or dialkyl peroxides (ROOR') leading to

301 HOMs. However, negligible products relevant to HOMs were detected in our experiments,

302 indicating a minor importance for the self- and cross-reactions of RO_2 compared to the competing

303 reactions between RO_2 and $HO_2/NO/RO_2$ to form ring-opening products. Our results for

304 insignificant contribution of HOMs to SOA formation from m-xylene oxidation are consistent with

305 a small yield of HOMs reported in a previous study (Molteni et al., 2018).

306   We simulated the time-dependent evolution of the gaseous products by employing a tri-

307 exponential kinetic model (Fig. 1b and Table S1). Multi-generation oxidation of m-xylene occurs

308 via consecutive reaction steps to produce a multi-generation product, P_n (where n denotes the

309 sequence of OH oxidation), which subsequently engages in additional OH oxidation, wall loss,

310 and aerosol loss. Fig. 1b-d indicates that the simulated concentrations well reproduce those

311 measured for P_1 to P_3 by adopting our measured γ (to be discussed below) and estimated wall loss

312 rates (see Methods and Table S1 in SI).

313 **3.2   Particle size growth, SSA, and chemical speciation**

314   To evaluate SOA and BrC formation from COOs, we measured the time-dependent GF,

315 SSA, and density, after $(NH_4)_2SO_4$ seed particles are exposed to the m-xylene oxidation products

316 in the presence of 19 ppb NH_3 and at 70% RH (Fig. 2a-c, Exp. 1). The GF increases monotonically

317 and reaches a value of (2.41 ± 0.03) at 120 min (Fig. 2a), while the SSA declines steadily

318   throughout the exposure and reaches the value of (0.91 ± 0.01) at 120 min (Fig. 2b). The latter is

319   indicative of the production of light-absorbing BrC. The measured SSA for *m*-xylene is lower than

320   that previously reported for toluene under comparable experimental conditions (Li et al., 2021b).

321   The difference in SSA/BrC formation between toluene and *m*-xylene is explained by a higher yield

322   of methylglyoxal from *m*-xylene than from toluene (Jenkin et al., 2003; Nishino et al., 2010), since

323   methylglyoxal produces BrC more efficiently via aqueous reaction than glyoxal (Li et al., 2021a).

324   Analysis of particle chemical composition using TD-ID-CIMS reveals high abundances of

325   oligomers, nitrogen-containing organics (NCO) consisting of N-heterocycles/N-heterochains,

326   carboxylates, along with a small amount of dimethylresorcinol/benzoquinone (Fig. 2c). The

327   identified mass peaks are summarized in Tables S2 to S4. Assuming similar sensitivity to proton-

328   transfer reactions for the aerosol-phase organics, i.e., with the proton transfer reaction rate

329   constants of (2 to 4) $\times$ 10^{-9} cm^3 $molecule^{-1}$ s^{-1} (Zhao and Zhang, 2004), the contributions of

330   oligomers, NCO, carboxylates, and dimethylresorcinol/benzoquinone to the total SOA formation

331   are estimated to be 22%, 23%, 47%, and 8%, respectively, at 70% RH (Table S5). Note that the

332   TD-ID-CIMS method preserves the identify for all organic species without fragmentation,

333   providing unambiguous chemical speciation for the aerosol-phase products.

334   **3.3   Effects of seed particles, NH_3, RH, and NO_x**

335   We assessed the dependence of SOA/BrC formation from *m*-xylene-OH oxidation on

336   different seed particles (Exp. 1-4), NH_3 concentration (Exp. 1-12), RH (Exp. 1,13-15), and NO_x

337   concentration (Exp. 1,16-18). Fig. 3a shows that $(NH_4)_2SO_4$ in the presence of 19 ppb NH_3 exhibits

338   the largest GF and lowest SSA at 120 min, which are explained by the chemical mechanisms

339   leading to the formation of the observed aerosol-phase products. While dicarbonyls undergo

340   aqueous phase reactions to form oligomers (Fig. S4) (Ji et al., 2020; Li et al., 2021a), organic acids

341   engage in ionic dissociation and acid-base reaction to yield carboxylates (Fig. 3b). In addition, the

342   reaction of dicarbonyls with NH_3 produces N-heterocycles/N-heterochains (Fig. S5), which are

343   light-absorbing (Marrero-Ortiz et al., 2019; Li et al., 2021a). Oligomerization of dicarbonyls

344   involves protonation, hydration, and deprotonation, which are mediated by carbenium ions via

345   nucleophilic addition (Ji et al., 2020; Li et al., 2021a). While protonation of dicarbonyls to yield

346   carbenium ions is promoted by hydrogen ion activity, high acidity hinders hydration and

347   deprotonation, explaining the largest GF and the smallest SSA on weakly acidic $(NH_4)_2SO_4$

348   particles in the presence NH_3 (Fig. 3a). In addition, uptake of dicarbonyls, organic acids, and PAQ

349   is likely facilitated on aqueous $(NH_4)_2SO_4$ particles, because of surface propensity of charge-

350   separation at the interface (Hua et al., 2011; Shi et al., 2020). Specifically, surface-abundant NH_4^+

351   cations arising from interfacial charge separation of $(NH_4)_2SO_4$ likely exert electrostatic attraction

352   to gaseous oxygenated species (with a negative charge character) to enhance uptake for

353   dicarbonyls, organic acids, and PAQ (Li et al., 2021a,b). The most efficient formation of SOA and

354   BrC on $(NH_4)_2SO_4$ particles in the presence of NH_3 are also consistent with the measured highest

355   intensities for oligomers and NCO (Fig. 3b). On the other hand, ionic dissociation and acid-base

356   reaction to yield carboxylates occur efficiently in the presence of NH_3/NaCl, as evident from the

357   increasing carboxylate intensity from NH_4HSO_4 to NaCl (Fig. 3b). The GF and SSA increase and

358   decrease, respectively, with NH_3 from 0 to 27 ppb for all three types of seed particles (Fig. 4a,b),

359   relevant to the reactions of NH_3 with dicarbonyls to form NCO and with organic acids to form

360   ammonium carboxylates. The analysis of the particle composition confirms that the intensities of

361   oligomers, NCO, and carboxylates increase with the NH_3 concentration (Fig. 4c-e).

362   We carried out additional experiments by varying RH from 10% to 70% in the presence of

363   19 ppb NH_3 (Fig. 5). The GF decreases with increasing RH from (3.10 ± 0.06) at RH = 10% to

364   (2.41 ± 0.03) at RH = 70% (Fig. 5a). The measured SSA at 120 min is close to unity at 10% and

365   30% RH and decreases with increasing RH (Fig. 5a), indicating negligible NCO formation at low

366   RH but significant NCO formation at RH above 50%. Carboxylates represent the dominant

367   constituent throughout the RH range (i.e., 85% at 10% RH to 47% at 70% RH), while the

368   contributions of oligomers and NCO are small at low RH (2-5% at RH < 40%) and become

369   increasingly significant at high RH (15-23% at RH > 50%) (Fig. 5b). The fraction for PAQ (8%)

370   is nearly invariant with RH. For $(NH_4)_2SO_4$ particles, the deliquescent and efflorescent points are

371   at 80% and 36% RH, respectively (Li et al., 2021b). At low RH (10% and 30%), aqueous reactions

372   to yield oligomers/NCO are minimal because of small water activity and significantly suppressed

373   protonation and oligomerization. On the other hand, carboxylic acids readily undergo ionic

374   dissociation or acid-base reaction, since organic acids efficiently retain water even at low RH (Xue,

375   2009). The equilibrium vapor pressures for PAQ are much lower than those for organic acids

376   (Table S6), facilitating more efficient condensation. Additionally, wall-loss of COOs is more

377   pronounced at high RH (Li et al., 2021b), explaining the decreased GF with increasing RH.

378   Measurement of gaseous concentrations for COOs shows that wall-loss is 1.5 to 4.6 times more

379   efficient at 70% RH than at 10% RH, while wall loss of *m*-xylene is negligible at both RH levels

380   (Table S7).

381   We determined the total density and the density of the SOA fraction for $(NH_4)_2SO_4$ seed

382   particles exposed to *m*-xylene oxidation (Fig. 5 c,d). The measured densities are distinct between

383   10 and 70% RH. At 10% RH, the total density decreases monotonically, while the SOA density

384   increases slightly with reaction time, i.e., from 1.27 to 1.39 g cm^{-3} (Fig. 5c), indicating minor

385   oligomers and dominant carboxylic acids at low RH. At 70% RH, the total particle density initially

386   decreases from 1.77 g cm^{-3} to 1.41 g cm^{-3} (at a GF of 1.24) and subsequently increases steadily to

387   1.56 g cm^{-3} at 120 min. The SOA density on $(NH_4)_2SO_4$ particles increases from 1.26 g cm^{-3} at 10

388   min to 1.55 g cm^{-3} at 120 min (Fig. 5d). The evolution in the densities reflects the variation in the

389   chemical composition. The initial particle growth is dominated by small oligomers, imidazoles

390   from methylglyoxal/methylbutenedial, and early-generation organic acids (e.g., toluic acid), with

391   the densities from 0.98 to 1.27 g cm^{-3} (Table S8). Subsequent particle growth from

392   methylglyoxal/methylbutenedial yields large oligomers, with the densities of 1.71-1.90 g cm^{-3}

393   (Table S8).

394   To evaluate the NO_x effects, we performed experiments on $(NH_4)_2SO_4$ seed particles by

395   varying the initial NO_x concentration from 0 to 500 ppb (Fig. 6). Three major nitrophenols are

396   identified from NO_2 addition to the OH-m-xylene adduct, i.e., 4-methyl-2-nitrophenol ($m/z = 154$),

397   dimethyl nitrophenol ($m/z = 168$), and dimethyl-4-nitrocatechol ($m/z = 184$) (Fig. 6a). The

398   production of nitrophenols is much smaller than those for dicarbonyls and organic acids, consistent

399   with a smaller yield (less than 7%) for nitrophenols (Fan and Zhang, 2008). The GF on $(NH_4)_2SO_4$

400   seed particles with NH_3 decreases from 2.41 ± 0.03 to 2.18 ± 0.03 with 0 to 500 ppb NO_x (Fig. 6b).

401   The SSA decreases significantly from 0.911 ± 0.006 to 0.839 ± 0.003 with increasing NO_x (Fig.

402   6b), because of the formation of light-absorbing nitrophenols (Hems and Abbatt, 2018; Li et al.,

403   2021b). Analysis of particle composition reveals that the decreasing GF with increasing NO_x

404   correlates with simultaneous decreases of carboxylates, oligomers, and NCOs and with increasing

405   nitrophenols in the aerosol-phase (Fig. 6c). Overall, nitrophenols contribute 2% to 4% to the SOA

406   formation. Addition of NO_x not only produces nitrophenols and but also alters the cycling between

407   RO_2 and alkoxy (RO) radicals, leading to re-distributions of COOs. The presence of NO_x decreases

408   dicarbonyls and organic acids, as evident from decreased intensities for oligomers, NCO, and

409   carboxylates in the aerosol-phase with increasing NO_x (Fig. 2h).

3.4 COO and SOA Yields

From the measured GF and COO concentrations, we derived the γ, which is widely employed to represent aerosol formation in atmospheric models (Zhang et al., 2015). The measured γ varies with the functionality of COOs and RH on $(NH_4)_2SO_4$ seed particles (Fig. 7a). Results of the γ values for COOs are also summarized in Table S9. The γ for dicarbonyls is the highest (from 3×10^{-3} to 1.3×10^{-2}) at 70% RH but is significantly reduced (from 3.7×10^{-4} to 1.0×10^{-3}) at 10% RH, while the γ's for organic acids, PAQ, and nitrophenols are slightly higher at 70% RH. Among the organic acids, the γ correlates with the acid dissociation constant and solubility, which are the highest for pyruvic acid and the lowest for toluic acid. The standard variation in γ (within one σ) among each COO type is within 50%, 40%, 30%, and 15% for dicarbonyls, organic acids, PAQ, and nitrophenols, respectively. From the measured concentrations of COOs and *m*-xylene, we determined the COO yields (Y_{COO}) using eq. 17, by considering four COO species, i.e., dicarbonyls for $i = 1$, carboxylic acids for $i = 2$, PAQ for $i = 3$, and nitrophenols for $i = 4$ (Table S7). The Y_{COO} values for dicarbonyls, organic acids, PAQ, and nitrophenols are 25%, 37%, 5%, and 3%, respectively (Fig. 7b), indicating significant production of COOs from *m*-xylene oxidation.

Our work shows significant increase in particle size (Fig. 2a) and constantly varying particle properties, i.e., SSA (Fig. 2b) and density (Fig. 5c,d), which closely correlate with the gaseous COO production (Fig. 1). These results imply a highly nonequilibrium kinetic process leading to SOA formation from m-xylene oxidation, which cannot be described by equilibrium partitioning. The gas-to-particle conversion from *m*-xylene oxidation is dominated by several volatile COO species (i.e., organic acids and dicarbonyls) and with minor contribution from condensation of low-volatility COO (i.e., polyhydroxy aromatics/quinones, and nitrophenols) (Fig.

In our study, the vapor pressures of the detected gaseous oxidation products for organic acids

and dicarbonyls are too large to explain the measured particle growth via equilibrium partitioning

(Table S6). Specifically, the saturation vapor pressures of organic acids detected in the particle-

phase range from 1.9×10^{-3} to 6.6×10^{-6} atm, while their gas-phase concentrations range from 0.5

to 2.5 ppb. Similarly, the saturation vapor pressures of dicarbonyls detected in the particle-phase

range from 1.6×10^{-1} to 3.9×10^{-4} atm, while their gas-phase concentrations range from 0.5 to 2.2

ppb. The high saturation vapor pressures and low gas-phase concentrations for those COOs render

equilibrium partitioning implausible in our experiments. Also, the detection of the particle-phase

products confirms that organic acids and dicarbonyls directly participate in heterogeneous

reactions to yield low-volatility products. Moreover, volatility-based equilibrium partitioning

cannot not explain the variations in the particle size growth, SSA, and chemical compositions on

different seed particles (Fig. 3). Clearly, the gas-to-particle conversion from m-xylene oxidation

involves several distinct heterogeneous processes, including the interfacial interaction, ionic

dissociation/acid-base reaction, and nucleophilic oligomerization (Li et al., 2021a,b).

We establish a functionality-based SOA formation to predict the aerosol mass

concentration (M_{SOA}) from the measured gaseous concentrations and γ's for COOs using eq. 20.

The M_{SOA} is calculated using the averaged γ (Fig. 7a and Table S10) and the measured time-

averaged concentrations for each COO type (Table S7). While the production of COOs is

dependent on the VOC types and photooxidation, the aerosol-phase reactivity of COOs, as

represented by γ, is only dependent on the functionality for a given aerosol type. Thus, SOA

formation from various VOC types can be predicted from the production and reactivity for COOs

based on the experimental measurements, by categorizing COOs in accordance with their

functional groups. In our study, the measured uptake coefficient for each COO type (γ_i) is derived

456   from the measured particle growth (eqs. 9 and 10), which implicitly accounts for non-continuum

457   diffusion, imperfect accommodation, and evaporation (Zhang et al., 1994; Ravishankara, 1997).

458   To assess the consistency of our approach, we compared the predicted and measured SOA

459   mass yields (Y_{SOA}), according to eq. 21. The predicted Y_{SOA} is (11 ± 3)% and (6 ± 1)%,

460   respectively, at 10% and 70 % RH, comparable to the measured values of (14 ± 0.4)% and (6.3 ±

461   0.2)% on $(NH_4)_2SO_4$ seed particles (Fig. 7c). The slight differences between the predicted and

462   measured Y_{SOA}'s are explainable by the uncertainties related to lumping each COO type (i.e.,

463   averaging the γ values) as well as unaccounted low-abundant COO species. To account for the

464   RH-dependent wall loss for COOs, we corrected Y_{SOA} from the measured gaseous concentrations

465   at varying RH (see Methods and Table S7). Such correction results in an increase of about one to

466   four times for Y_{SOA} at 10% and 70% RH, yielding the values of (20 ± 4)% and (32 ± 7)%,

467   respectively (Fig. 7c). Under atmospheric conditions, SOA/BrC formation from *m*-xylene is

468   expected to be enhanced at high RH, because of significantly enhanced aqueous reaction, larger

469   aerosol surface-area, and higher water activity. Field measurements showed significantly enhanced

470   SOA formation with increasing RH during severe haze evolution (Guo et al., 2014; Peng et al.,

471   2021).

472   **4.   Conclusions**

473   In this work we have elucidated the production of COOs and their roles in SOA formation

474   from *m*-xylene oxidation. The major advantages of our analytical methodologies lie in

475   simultaneous monitoring of the evolutions of gaseous oxidation products and aerosol properties

476   when seed particles are exposed to the oxidation products, which allows for assessment of multi-

477   generation production of SOA and BrC. Also, our experimental approach remedies the deficiency

478   of wall loss of reactive gaseous and particles, which represents a main obstacle in experimental

479   investigation using environmental chambers (Zhang et al., 2014; Huang et al., 2018). OH-initiated

480   oxidation of *m*-xylene produces four distinct COO types consisting of dicarbonyls, carboxylic

481   acids, polyhydroxy aromatics/quinones, and nitrophenols from early-generation (P_2 and P_3), with

482   the yields of 25%, 37%, 5%, and 3%, respectively. SOA formation occurs via several

483   heterogeneous processes, including interfacial interaction, ionic dissociation/acid-base reaction,

484   and oligomerization, with the yields of $(20 \pm 4)\%$ at 10% RH and $(32 \pm 7)\%$ at 70% RH. The

485   identified aerosol-phase products include dominant oligomers, N-heterocycles/N-heterochains,

486   and carboxylates at high RH and dominant carboxylates at low RH, along with small amounts of

487   PAQ and nitrophenols (in the presence of NO_x). The nitrogen-containing organics consisting of

488   N-heterocycles, N-heterochains, and nitrophenols are light-absorbing, characterized by low SSA.

489   The measured γ for COOs is dependent on the functionality, ranging from 3.7×10^{-4} to 1.3×10^{-2}.

490   A kinetic framework is developed to predict SOA formation from the concentration and γ for

491   COOs. Our results illustrate that SOA formation from *m*-xylene oxidation is accurately quantified

492   from the abundance and reactivity for COOs (i.e., eq. 20). Notably, this kinetic framework

493   accounts for the interfacial process (i.e., mass accommodation) as well as aqueous reactions (i.e.,

494   oligomerization and acid-base reactions) without the assumption of gas-particle equilibrium. We

495   envisage that this functionality-based approach is applicable to predict SOA formation from VOC

496   photooxidation using experiment/field measured or model-simulated COOs, aerosol surface area,

497   and reactivity. We conclude that photochemical oxidation of *m*-xylene represents a major source

498   for SOA and BrC formation under urban conditions, because of its large abundance, high reactivity

499   with OH, and high yields for COOs.

500   **ACKNOWLEDGEMENTS**

REFERENCES

Atkinson, R. Atmospheric Chemistry of VOCs and NO_x. Atmos. Environ., 34, 2063–2101, 2000.

Calvert, J. G., Atkinson, R., Becker, K. H., Kamens, R. M., Seinfeld, J. H., Wallington, T. H., and Yarwood, G.: The Mechanisms of Atmospheric Oxidation of Aromatic Hydrocarbons, Oxford University Press: New York., 2002.

Claflin, M. S. and Ziemann, P. J.: Thermal desorption behavior of hemiacetal, acetal, ether, and ester oligomers, Aerosol Sci. Technol., 53(4), 473–484, doi:10.1080/02786826.2019.1576853, 2019.

Dotan, I., Albritton, D. L., Lindinger, W. and Pahl, M.: Mobilities of CO_2+, N_2H+, H_3O+, $H_3O+\cdot H_2O$, and $H_3O+\cdot(H_2O)_2$ ions in N_2, J. Chem. Phys., 65(11), 5028–5030, doi:10.1063/1.432943, 1976.

Fan, J., and Zhang, R.: Density Functional Theory Study on OH-Initiated Atmospheric Oxidation of m-Xylene, J. Phys. Chem. A, 112(18), 4314–4323, doi:10.1021/jp077648j, 2008.

Faust, J. A., Wong, J. P. S., Lee, A. K. Y., and Abbatt, J. P. D.: Role of Aerosol Liquid Water in Secondary Organic Aerosol Formation from Volatile Organic Compounds, Environ. Sci. Technol., 51, 1405− 1413, 2017.

Finlayson-Pitts, B. J., and Pitts, J. N.: Chemistry of the Upper and Lower Atmosphere: Theory, Experiments and Applications, Academic Press, San Diego, 2000.

Fortner, E. C., Zheng, J., Zhang, R., Berk Knighton, W., Volkamer, R. M., Sheehy, P., Molina, L., and André, M.: Measurements of Volatile Organic Compounds Using Proton Transfer Reaction – Mass Spectrometry during the MILAGRO 2006 Campaign, Atmos. Chem. Phys., 9(2), 467–481, doi:10.5194/acp-9-467-2009, 2009.

Fortner, E.C., Zhao, J., and Zhang, R.: Development of ion drift-chemical ionization mass spectrometry, Anal. Chem., 76, 5436-5440, 2004.

Fountoukis, C. and Nenes, A.: SORROPIA II: A Computationally Efficient Thermodynamic Equilibrium Model for $K+–Ca2+–Mg2+–NH4+–Na+–SO42−–NO3−–Cl–H_2O$ Aerosols., Atmos. Chem. Phys., 7(17), 4639–4659, doi:10.5194/acp-7-4639-2007, 2007.

Garmash, O., Rissanen, M. P., Pullinen, I., Schmitt, S., Kausiala, O., Tillmann, R., Zhao, D., Percival, C., Bannan, T. J., Priestley, M., Hallquist, Å. M., Kleist, E., Kiendler-Scharr, A., Hallquist, M., Berndt, T., McFiggans, G., Wildt, J., Mentel, T. F., and Ehn, M.: Multi-generation OH oxidation as a source for highly oxygenated organic molecules from aromatics, Atmos. Chem. Phys., 20(1), 515–537, doi:10.5194/acp-20-515-2020, 2020.

535 Guo, S., Hu, M., Zamora, M. L., Peng, J., Shang, D., Zheng, J., Du, Z., Wu, Z., Shao, M., Zeng,
536 L., Molina, M. J., and Zhang, R.: Elucidating severe urban haze formation in China, Proc. Natl.
537 Acad. Sci. USA, 111(49), 17373–17378, doi:10.1073/pnas.1419604111, 2014.

538 Guo, S., Hu, M., Lin, Y., Gomez-Hernandez, M., Zamora, M. L., Peng, J., Collins, D. R., and
539 Zhang, R.: OH-Initiated Oxidation of m-Xylene on Black Carbon Aging, Environ. Sci. Technol.,
540 50(16), 8605–8612, doi:10.1021/acs.est.6b01272, 2016.

541 Guo, S., Hu, M., Peng, J., Wu, Z., Zamora, M. L., Shang, D., Du, Z., Zheng, J., Fang, X., Tang,
542 R., Wu, Y., Zeng, L., Shuai, S., Zhang, W., Wang, Y., Ji, Y., Li, Y., Zhang, A. L., Wang, W.,
543 Zhang, F., Zhao, J., Gong, X., Wang, C., Molina, M. J. and Zhang, R.: Remarkable nucleation
544 and growth of ultrafine particles from vehicular exhaust, Proc. Natl. Acad. Sci., 117(7), 3427–
545 3432, doi:10.1073/pnas.1916366117, 2020.

546 De Haan, D. O., Hawkins, L. N., Kononenko, J. A., Turley, J. J., Corrigan, A. L., and Tolbert, M.
547 A., Jimenez, J. L.: Formation of Nitrogen- Containing Oligomers by Methylglyoxal and Amines
548 in Simulated Evaporating Cloud Droplets, Environ. Sci. Technol., 45, 984− 991, 2011.

549 De Haan, D. O., Hawkins, L. N., Welsh, H. G., Pednekar, R., Casar, J. R., Pennington, E. A., de
550 Loera, A., Jimenez, N. G., Symons, M. A., Zauscher, M., Pajunoja, A., Caponi, L., Cazaunau, M.,
551 Formenti, P., Gratien, A., Pangui, E., and Doussin, J.-F.: Brown Carbon Production in
552 Ammonium- or Amine-Containing Aerosol Particles by Reactive Uptake of Methylglyoxal and
553 Photolytic Cloud Cycling, Environ. Sci. Technol., 51(13), 7458–7466,
554 doi:10.1021/acs.est.7b00159, 2017.

555 Heald, C. L., Jacob, D. J., Park, R. J., Russell, L. M., Huebert, B. J., Seinfeld, J. H., Liao, H., and
556 Weber, R. J.: A Large Organic Aerosol Source in the Free Troposphere Missing from Current
557 Models. Geophys. Res. Lett., 32, 1−4, 2005.

558 Hems, R. F., and Abbatt, J. P. D.: Aqueous Phase Photo-oxidation of Brown Carbon Nitrophenols:
559 Reaction Kinetics, Mechanism, and Evolution of Light Absorption, ACS Earth Sp. Chem., 2(3),
560 225–234, doi:10.1021/acsearthspacechem.7b00123, 2018.

561 Hodzic, A., Kasibhatla, P. S., Jo, D. S., Cappa, C. D., Jimenez, J. L., Madronich, S., and Park, R.
562 J.: Rethinking the Global Secondary Organic Aerosol (SOA) Budget: Stronger Production, Faster
563 Removal, Shorter Lifetime. Atmos. Chem. Phys., 16, 7917−7941, 2016.

564 Hua, W., Jubb, A. M., and Allen, H. C.: Electric Field Reversal of Na2SO4, (NH4)2SO4, and
565 Na2CO3 Relative to CaCl2 and NaCl at the Air/Aqueous Interface Revealed by Heterodyne
566 Detected Phase-Sensitive Sum Frequency, J. Phys. Chem. Lett., 2(20), 2515–2520,
567 doi:10.1021/jz200888t, 2011.

568 Huang, Y., Zhao, R., Charan, S. M., Kenseth, C. M., Zhang, X., and Seinfeld, J. H.: Unified Theory
569 of Vapor–Wall Mass Transport in Teflon-Walled Environmental Chambers, Environ. Sci.
570 Technol., 52(4), 2134–2142, doi:10.1021/acs.est.7b05575, 2018.

Intergovernmental Panel on Climate Change (IPCC). *Climate Change 2013: The Physical Science Basis. Contribution of Working Group I to the Fifth Assessment Report of the Intergovernmental Panel on Climate Change*. Cambridge University Press, 2013.

Jenkin, M. E., Saunders, S. M., Wagner, V., and Pilling, M. J.: Protocol for the development of the Master Chemical Mechanism, MCM v3 (Part B): tropospheric degradation of aromatic volatile organic compounds, Atmos. Chem. Phys., 3(1), 181–193, doi:10.5194/acp-3-181-2003, 2003.

Ji, Y., Zhao, J., Terazono, H., Misawa, K., Levitt, N. P., Li, Y., Lin, Y., Peng, J., Wang, Y., Duan, L., Pan, B., Zhang, F., Feng, X., An, T., Marrero-Ortiz, W., Secrest, J., Zhang, A. L., Shibuya, K., Molina, M. J., and Zhang, R.: Reassessing the atmospheric oxidation mechanism of toluene, Proc. Natl. Acad. Sci. USA, 114(31), 8169–8174, doi:10.1073/pnas.1705463114, 2017.

Ji, Y., Shi, Q., Li, Y., An, T., Zheng, J., Peng, J., Gao, Y., Chen, J., Li, G., Wang, Y., Zhang, F., Zhang, A. L., Zhao, J., Molina, M. J., and Zhang, R.: Carbenium ion-mediated oligomerization of methylglyoxal for secondary organic aerosol formation, Proc. Natl. Acad. Sci. USA, 117(24), 13294 LP – 13299, doi:10.1073/pnas.1912235117, 2020.

Jia, L., and Xu, Y.: Effects of Relative Humidity on Ozone and Secondary Organic Aerosol Formation from the Photooxidation of Benzene and Ethylbenzene, Aerosol Sci. Technol., 48(1), 1–12, doi:10.1080/02786826.2013.847269, 2014.

Jia, L., and Xu, Y.: Different roles of water in secondary organic aerosol formation from toluene and isoprene, Atmos. Chem. Phys., 18(11), 8137–8154, doi:10.5194/acp-18-8137-2018, 2018.

Li, G., Zhang, R., Fan, J., and Tie, X.: Impacts of biogenic emissions on photochemical ozone production in Houston, Texas, J. Geophys. Res., 112, D10309, doi:10.1029/2006JD007924, 2007.

Li, Y., Ji, Y., Zhao, J., Wang, Y., Shi, Q., Peng, J., Wang, Y., Wang, C., Zhang, F., Wang, Y., Seinfeld, J. H., and Zhang, R.: Unexpected Oligomerization of Small α-Dicarbonyls for Secondary Organic Aerosol and Brown Carbon Formation, Environ. Sci. Technol., 55(8), 4430–4439, doi:10.1021/acs.est.0c08066, 2021a.

Li, Y., Zhao, J., Wang, Y., Seinfeld, J. H., and Zhang, R.: Multigeneration Production of Secondary Organic Aerosol from Toluene Photooxidation, Environ. Sci. Technol., 55, 8592−8603, doi:10.1021/acs.est.1c02026, 2021b.

Liu, J., Zhang, F., Xu, W., Sun, Y., Chen, L., Li, S., Ren, J., Hu, B., Wu, H., and Zhang, R.: Hygroscopicity of Organic Aerosols Linked to Formation Mechanisms, Geophys. Res. Lett., 48(4), e2020GL091683, doi:https://doi.org/10.1029/2020GL091683, 2021.

Marrero-Ortiz, W., Hu, M., Du, Z., Ji, Y., Wang, Y. Y., Guo, S., Lin, Y., Gomez-Hermandez, M., Peng, J., Li, Y., Secrest, J., Zamora, M. L., Wang, Y. Y., An, T., and Zhang, R.: Formation and Optical Properties of Brown Carbon from Small α-Dicarbonyls and Amines, , 53(1), 117–126, doi:10.1021/acs.est.8b03995, 2019.

McMurry, P. H. and Rader, D. J.: Aerosol Wall Losses in Electrically Charged Chambers, Aerosol Sci. Technol., 4(3), 249–268, doi:10.1080/02786828508959054, 1985.

Molina, L. T.: Introductory lecture: air quality in megacities, Faraday Discuss, 226, 9-52, 10.1039/d0fd00123f, 2021.

Moise, T., Flores, J. M., and Rudich, Y.: Optical Properties of Secondary Organic Aerosols and Their Changes by Chemical Processes, Chem. Rev., 115, 4400−4439, 2015.

Molteni, U., Bianchi, F., Klein, F., El Haddad, I., Frege, C., Rossi, M. J., Dommen, J., and Baltensperger, U.: Formation of highly oxygenated organic molecules from aromatic compounds, Atmos. Chem. Phys., 18(3), 1909–1921, doi:10.5194/acp-18-1909-2018, 2018.

National Academies of Sciences Engineering and Medicine (NASEM): The Future of Atmospheric Chemistry Research: Remembering Yesterday, Understanding Today, Anticipating Tomorrow, The National Academies Press, Washington, DC., 2016.

Ng, N. L., Kroll, J. H., Chan, A. W. H., Chhabra, P. S., Flagan, R. C., and Seinfeld, J. H.: Secondary organic aerosol formation from m-xylene, toluene, and benzene, Atmos. Chem. Phys., 7(14), 3909–3922, doi:10.5194/acp-7-3909-2007, 2007.

Nishino, N., Arey, J., and Atkinson, R.: Formation Yields of Glyoxal and Methylglyoxal from the Gas-Phase OH Radical-Initiated Reactions of Toluene, Xylenes, and Trimethylbenzenes as a Function of NO2 Concentration, J. Phys. Chem. A, 114(37), 10140–10147, doi:10.1021/jp105112h, 2010.

Peng, J., Hu, M., Shang, D., Wu, Z., Du, Z., Tan, T., Wang, Y., Zhang, F., and Zhang, R.: Explosive secondary aerosol formation during severe haze in the North China Plain, Environ. Sci. Technol., 55(4), 2189–2207, 2021.

Pope, C. A., III, Burnett, R. T., Thun, M. J., Calle, E. E., Krewski, D., Ito, K., and Thurston, G. D.: Lung Cancer, Cardiopulmonary Mortality, and Long-Term Exposure to Fine Particulate Air Pollution. J. Am. Med. Assoc., 287, 1132−1141, 2002.

Qi, X., Zhu, S., Zhu, C., Hu, J., Lou, S., Xu, L., Dong, J. and Cheng, P.: Smog chamber study of the effects of NOx and NH3 on the formation of secondary organic aerosols and optical properties from photo-oxidation of toluene, Sci. Total Environ., 727, 138632, doi:https://doi.org/10.1016/j.scitotenv.2020.138632, 2020.

Ravishankara, A.R.: Heterogeneous and multiphase chemistry in the troposphere, Science 276, 1058-1065, 1997.

Schwantes, R. H., Schilling, K. A., McVay, R. C., Lignell, H., Coggon, M. M., Zhang, X., Wennberg, P. O., and Seinfeld, J. H.: Formation of highly oxygenated low-volatility products from cresol oxidation, Atmos. Chem. Phys., 17(5), 3453–3474, doi:10.5194/acp-17-3453-2017, 2017.

Seinfeld, J. H., and Pandis, S. N.: Atmospheric chemistry and physics: from air pollution to climate change, John Wiley & Sons., 2016.

Shi, Q., Zhang, W., Ji, Y., Wang, J., Qin, D., Chen, J., Gao, Y., Li, G., and An, T.: Enhanced uptake of glyoxal at the acidic nanoparticle interface: implications for secondary organic aerosol formation, Environ. Sci. Nano, 7, 1126−1135, 2020.

Shrivastava, M., Cappa, C. D., Fan, J., Goldstein, A. H., Guenther, A. B., Jimenez, J. L., Kuang, C., Laskin, A., Martin, S. T., Ng, N. L., Petaja, T., Pierce, J. R., Rasch, P. J., Roldin, P., Seinfeld, J. H., Shilling, J., Smith, J. N., Thornton, J. A., Volkamer, R., Wang, J., Worsnop, D. R., Zaveri, R. A., Zelenyuk, A., and Zhang, Q.: Recent advances in understanding secondary organic aerosol: Implications for global climate forcing, Rev. Geophys., 55(2), 509–559, doi:10.1002/2016RG000540, 2017.

Song, C., Na, K., Warren, B., Malloy, Q., and Cocker, D. R.: Secondary Organic Aerosol Formation from m-Xylene in the Absence of NOx, Environ. Sci. Technol., 41(21), 7409–7416, doi:10.1021/es070429r, 2007.

Suh, I., Lei, W., and Zhang, R.: Experimental and theoretical studies of isoprene reaction with NO_3, J. Phys. Chem., 105, 6471-6478, 2001.

Tan, Y., Lim, Y. B., Altieri, K. E., Seitzinger, S. P., and Turpin, B. J.: Mechanisms leading to oligomers and SOA through aqueous photooxidation: insights from OH radical oxidation of acetic acid and methylglyoxal, Atmos. Chem. Phys., 11, 18319−18347, 2012.

Wang, G., Zhang, F., Peng, J., Duan, L., Ji, Y., Marrero-Ortiz, W., Wang, J., Li, J., Wu, C., Cao, C., Wang, Y., Zheng, J., Secrest, J., Li, Y., Wang, Y., Li, H., Li, N., and Zhang, R.: Particle acidity and sulfate production during severe haze events in China cannot be reliably inferred by assuming a mixture of inorganic salts, Atmos. Chem. Phys., 18, 10123–10132, doi: 10.5194/acp-18-10123-2018, 2018.

Wang, L., Khalizov, A. F., Zheng, J., Xu, W., Ma, Y., Lal, V. and Zhang, R.: Atmospheric nanoparticles formed from heterogeneous reactions of organics, Nat. Geosci., 3(4), 238–242, doi:10.1038/ngeo778, 2010.

Wang, M., Chen, D., Xiao, M., Ye, Q., Stolzenburg, D., Hofbauer, V., Ye, P., Vogel, A. L., Mauldin, R. L., Amorim, A., Baccarini, A., Baumgartner, B., Brilke, S., Dada, L., Dias, A., Duplissy, J., Finkenzeller, H., Garmash, O., He, X.-C., Hoyle, C. R., Kim, C., Kvashnin, A., Lehtipalo, K., Fischer, L., Molteni, U., Petäjä, T., Pospisilova, V., Quéléver, L. L. J., Rissanen, M., Simon, M., Tauber, C., Tomé, A., Wagner, A. C., Weitz, L., Volkamer, R., Winkler, P. M., Kirkby, J., Worsnop, D. R., Kulmala, M., Baltensperger, U., Dommen, J., El-Haddad, I., and Donahue, N. M.: Photo-oxidation of Aromatic Hydrocarbons Produces Low-Volatility Organic Compounds, Environ. Sci. Technol., 54(13), 7911–7921, doi:10.1021/acs.est.0c02100, 2020.

Wang, Y., Khalizov, A., Levy, M., and Zhang, R.: Light absorbing aerosols and their atmospheric impacts, Atmos. Environ., 81, 713-715, doi:10.1016/j.atmosenv.2013.09.034, 2013.

Wang, Y., Lee, K.-H., Lin, Y., Levy, M., and Zhang, R.: Distinct effects of anthropogenic aerosols on tropical cyclones, Nature Clim. Change, 4, 368–373, doi:10.1038/nclimate2144 2014.

Wennberg, P. O., Bates, K. H., Crounse, J. D., Dodson, L. G., McVay, R. C., Mertens, L. A., Nguyen, T. B., Praske, E., Schwantes, R. H., Smarte, M. D., St Clair, J. M., Teng, A. P., Zhang, X., and Seinfeld, J. H.: Gas-Phase Reactions of Isoprene and Its Major Oxidation Products, Chem. Rev., 118, 3337–3390, 2018.

Xue, H., Khalizov, A. F., Wang, L., Zheng, J., and Zhang, R.: Effects of Coating of Dicarboxylic Acids on the Mass−Mobility Relationship of Soot Particles, Environ. Sci. Technol., 43(8), 2787–2792, doi:10.1021/es803287v, 2009.

Yuan, B., Koss, A. R., Warneke, C., Coggon, M., Sekimoto, K. and de Gouw, J. A.: Proton-Transfer-Reaction Mass Spectrometry: Applications in Atmospheric Sciences, Chem. Rev., 117(21), 13187–13229, doi:10.1021/acs.chemrev.7b00325, 2017.

Zhang, D., Lei, W., and Zhang, R.: Mechanism of OH formation from ozonolysis of isoprene: Kinetics and product yields, Chem. Phys. Lett. 358, 171-179, 2002.

Zhang, F., Wang, Y., Peng, J., Chen, L., Sun, Y., Duan, L., Ge, X., Li, Y., Zhao, J., Liu, C., Zhang, X., Zhang, G., Pan, Y., Wang, Y., Zhang, A.L., Ji, Y., Wang, G., Hu, M., Molina, M.J., and Zhang, R.: An unexpected catalyst dominates formation and radiative forcing of regional haze, Proc. Natl. Acad. Sci. USA, 117, 3960-3966, doi/10.1073/pnas.1919343117, 2020.

Zhang, Q., Xu, Y., and Jia, L.: Secondary organic aerosol formation from OH-initiated oxidation of m-xylene: effects of relative humidity on yield and chemical composition, Atmos. Chem. Phys., 19(23), 15007–15021, doi:10.5194/acp-19-15007-2019, 2019.

Zhang, R., Leu, M.T., and Keyser, L.F.: Heterogeneous reactions involving $ClONO_2$, HCl, and HOCl on liquid sulfuric acid surfaces, J. Phys. Chem., 98, 13563-13574, 1994.

Zhang, R., Suh, I., Zhao, J., Zhang, D., Fortner, E. C., Tie, X., Molina, L. T. and Molina, M. J.: Atmospheric New Particle Formation Enhanced by Organic Acids, Science (80-.)., 304(5676), 1487 LP – 1490, doi:10.1126/science.1095139, 2004.

Zhang, R., Wang, L., Khalizov, A. F., Zhao, J., Zheng, J., McGraw, R. L., and Molina, L. T.: Formation of nanoparticles of blue haze enhanced by anthropogenic pollution, Proc. Natl. Acad. Sci. USA, 106, doi:10.1073/pnas.0910125106, 17650-17654, 2009.

Zhang, R., Wang, G., Guo, S., Zamora, M. L., Ying, Q., Lin, Y., Wang, W., Hu, M., and Wang, Y.: Formation of Urban Fine Particulate Matter, Chem. Rev., 115(10), 3803–3855, doi:10.1021/acs.chemrev.5b00067, 2015.

Zhang, R., Johnson, N.M., and Li Y.: Establishing the exposure-outcome relation between airborne particulate matter and children's health, Thorax, 76, doi.org/10.1136/thoraxjnl-2021-217017, 2021.

Zhang, X., Cappa, C. D., Jathar, S. H., McVay, R. C., Ensberg, J. J., Kleeman, M. J., and Seinfeld, J. H.: Influence of Vapor Wall Loss in Laboratory Chambers on Yields of Secondary Organic Aerosol. Proc. Natl. Acad. Sci. U.S.A., 111, 5802−5807, 2014.

Zhao, J., and Zhang, R.: Proton transfer reaction rate constants between hydronium ion (H_3O^+) and volatile organic compounds, Atmos. Environ., 38(14), 2177–2185, doi:https://doi.org/10.1016/j.atmosenv.2004.01.019, 2004.

Zhao, J., Zhang, R., Fortner, E.C., and North, S.W.: Quantification of hydroxycarbonyls from OH-isoprene reactions, J. Am. Chem. Soc., 126, 2686-2687, 2004.

719 Zhao, J., Zhang, R., Misawa, K., and Shibuya, K.: Experimental product study of the OH-initiated
720 oxidation of m-xylene, J. Photochem. Photobiol. A Chem., 176(1), 199–207,
721 doi:https://doi.org/10.1016/j.jphotochem.2005.07.013, 2005.

722 Zhu, J., Penner, J. E., Lin, G., Zhou, C., Xu, L., and Zhuang, B.: Mechanism of SOA formation
723 determines magnitude of radiative effects, P. Natl. Acad. Sci. USA, 114, 12685–12690,
724 https://doi.org/10.1073/pnas.1712273114, 2017.

725

726
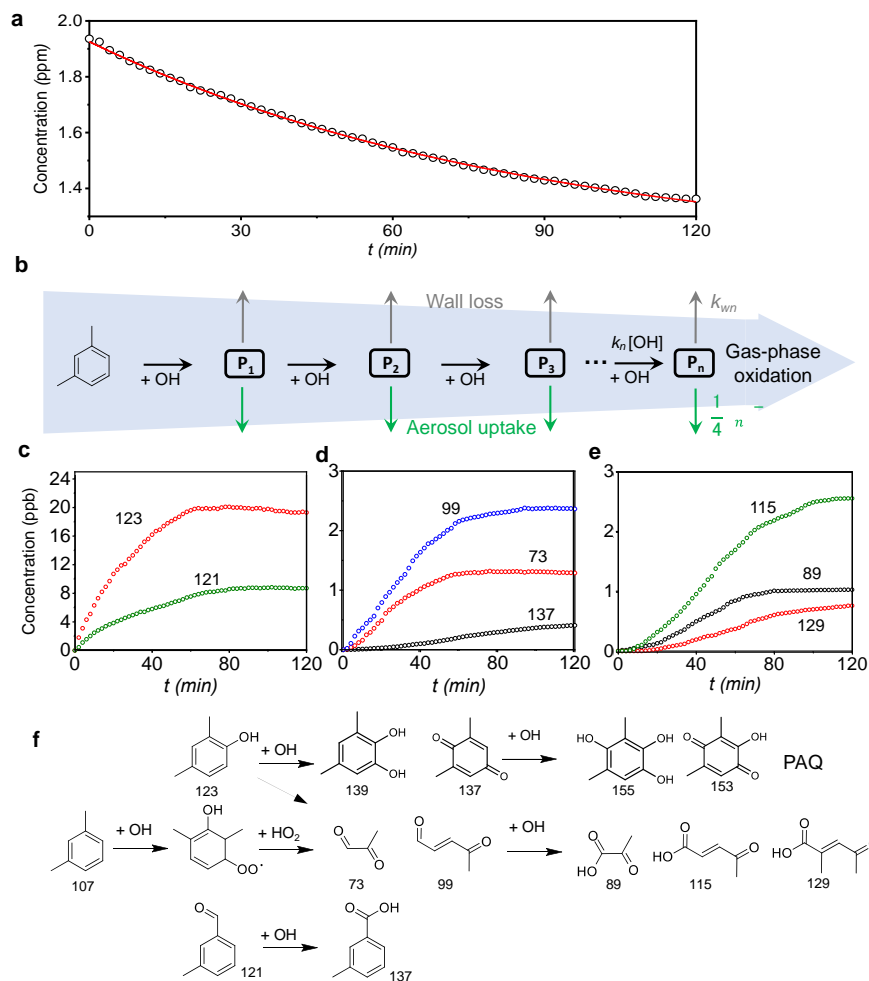
727
Figure 1. OH-initiated photooxidation of *m*-xylene. (a) Time-dependent concentration of *m*-xylene. The symbols are from the measurements, and the red solid line corresponds to exponential fitting of the *m*-xylene concentration. The initial concentration for *m*-xylene and the estimated steady-state concentration for OH are 1940 ppb and 2.1×10^6 molecules cm^{-3}, respectively, with a bimolecular rate constant of 2.4×10^{-11} cm^3 $molecule^{-1}$ s^{-1}. (b) Schematic representation leading to the multi-generation product, P_n, where *n* denotes the sequence of OH-initiated oxidation. The black, gray, and green arrows denote the gas-phase oxidation, chamber wall loss, and aerosol uptake, respectively. k_n and kw_n are the rate coefficients for the gas-phase oxidation and wall loss, respectively, γ_n represents the aerosol uptake coefficient, $\bar{c}$ is the thermal velocity, and *S* is the aerosol surface area. (c-e) Time-dependent gas-phase concentrations of P_1 (c), P_2 (d), and P_3 (e) products. The symbols are from measurements, and the solid curves are simulated according to the tri-exponential kinetics. (f) The gaseous oxidation pathways leading to the detected products. The top row corresponds to the pathways leading to polyhydroxy aromatics/quinones (PAQ). The numbers in (c) to (f) represents the mass to charge ratio (*m/z*). All experiments are carried out for $(NH_4)_2SO_4$ seed particles with 19 ppb NH_3 at 298 K and RH = 70%. Initiation of photooxidation by ultraviolet light occurs at *t* = 0.
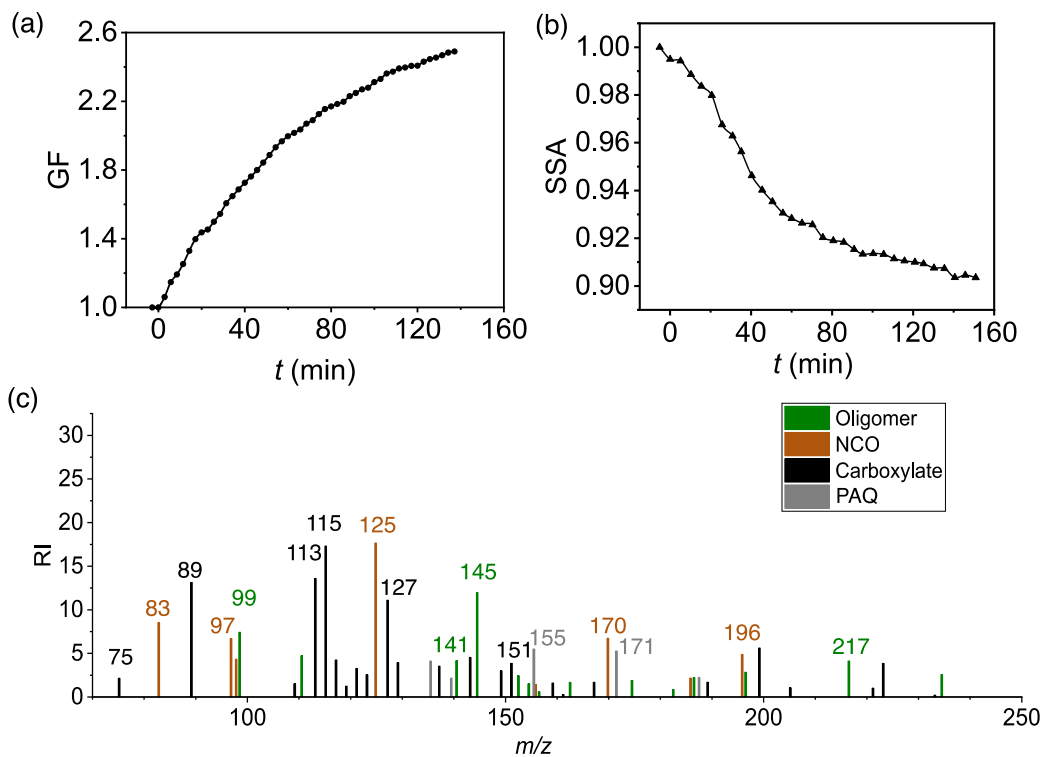
Figure 2. SOA and BrC formation from *m*-xylene photooxidation. Time-dependent growth factor (GF = D_p/D_0, a) and single scattering albedo (SSA, b) of seed particles exposed to *m*-xylene oxidation products. (c) Chemical speciation of aerosol-phase products by TD-ID-CIMS. Initiation of photooxidation by ultraviolet light occurred at $t = 0$. RI denotes the relative intensity for the integrated peak area during thermal desorption. All experiments are carried out for $(NH_4)_2SO_4$ seed particles with 19 ppb NH_3 at 298 K and RH = 70%.
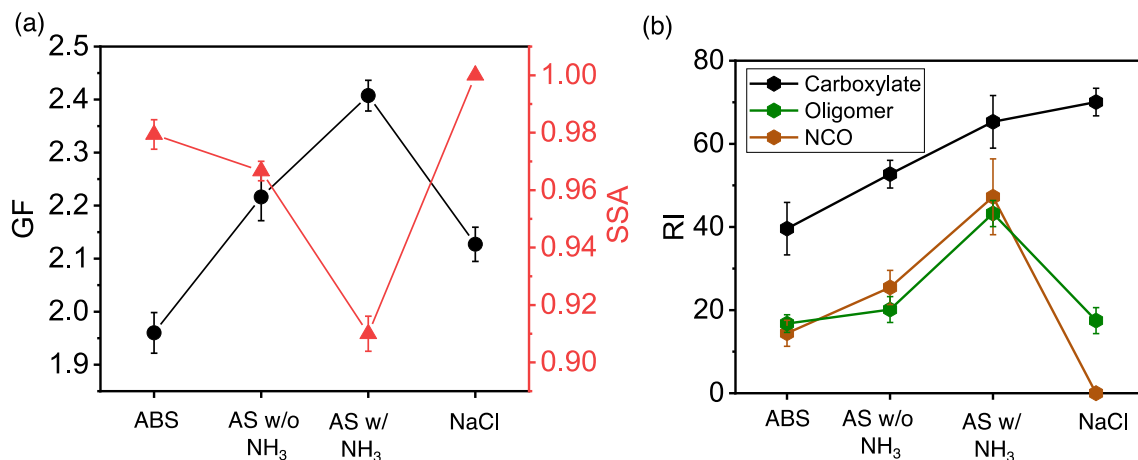
Figure 3. Dependence of SOA/BrC formation on seed particles. (a) GF (black) and SSA (red) at 120 mins of exposure for $(NH_4)_2SO_4$ particles in the presence (AS w/ NH_3) and absence (AS w/o NH_3) of 19 ppb NH_3 and for NH_4HSO_4 (ABS) and NaCl particles in the absence of NH_3. (b) Aerosol-phase relative intensity (RI) for carboxylates (black), oligomers (green), and NCO (brown) on different seed particles. The error bar denotes 1σ of 3 replicated measurements. All particle properties were measured relevant to dry conditions (less than 5% RH) and were dominantly contributed by non-volatile aerosol-phase products.
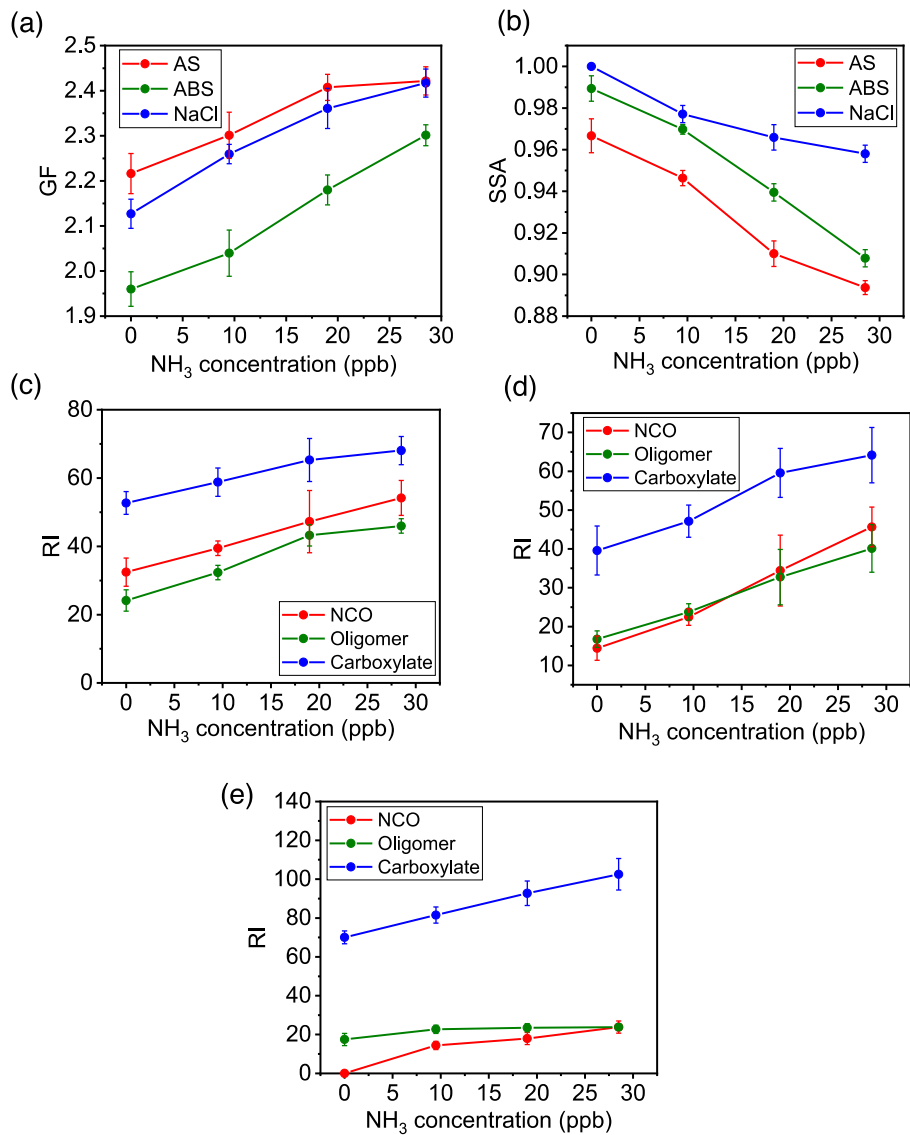
**Figure 4.** Variation of SOA formation with seed particles and NH₃ concentration. (a,b) growth factor (a) and SSA (b) at t = 120 min with varying NH₃ concentration between 0 and 27 ppb for ammonium sulfate (AS, red), ammonium bisulfate (ABS, green), and sodium chloride (NaCl, blue) seed particles. (c-e) Aerosol-phase mass relative intensity (RI) for NCO (red), oligomers (green), and carboxylates (blue) on AS (c), ABS (d), and NaCl (e) seed particles. The error bar denotes 1σ of 3 replicated measurements.
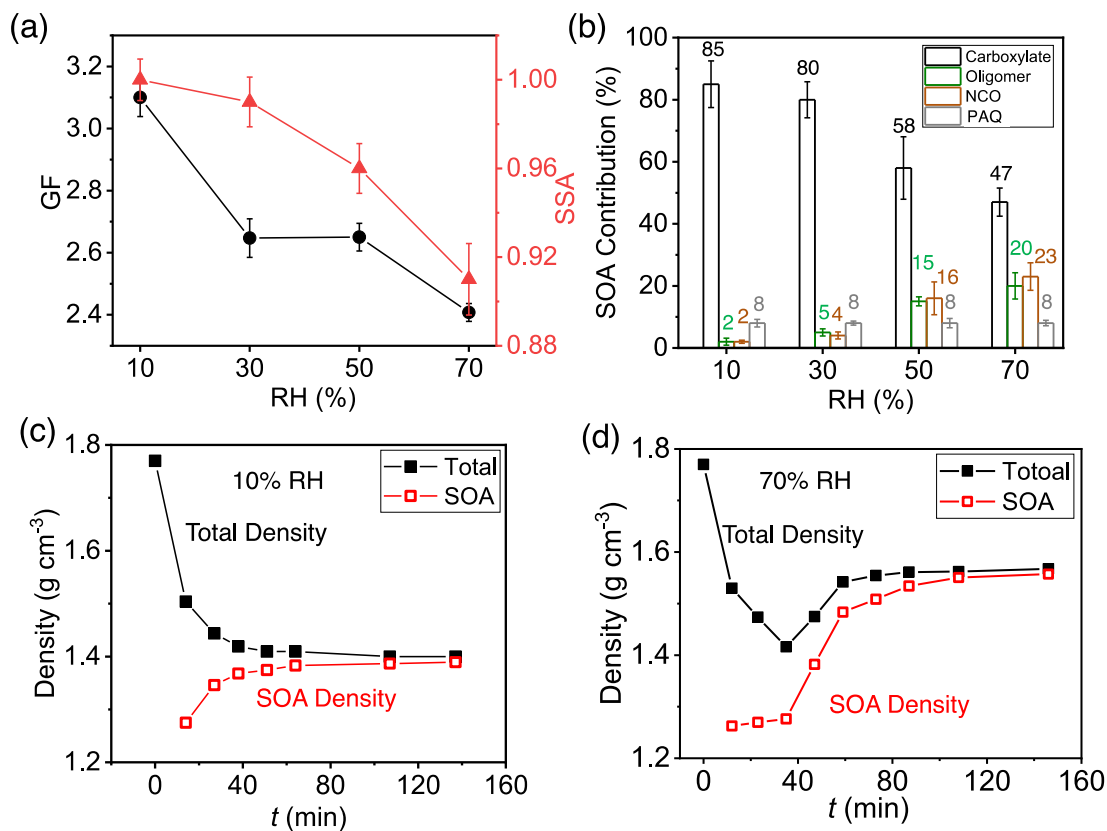
Figure 5. Dependence of SOA/BrC formation on RH. (a) GF (black) and SSA (red) at 120 min with varying RH from 10% to 70%. (b) Contribution of COOs to SOA formation with varying RH from 10% to 70%: carboxylate (black), oligomers (green), NCO (brown), and PAQ (gray) to SOA formation. The number denotes the percentage contribution (%) of each type of aerosol-phase products. (c,d) Time-dependent particle (black) and SOA (red) densities of seed particles exposed to *m*-xylene oxidation products at RH = 10% (c) and 70% (d), respectively. The error bar denotes 1σ of 3 replicated measurements.

35
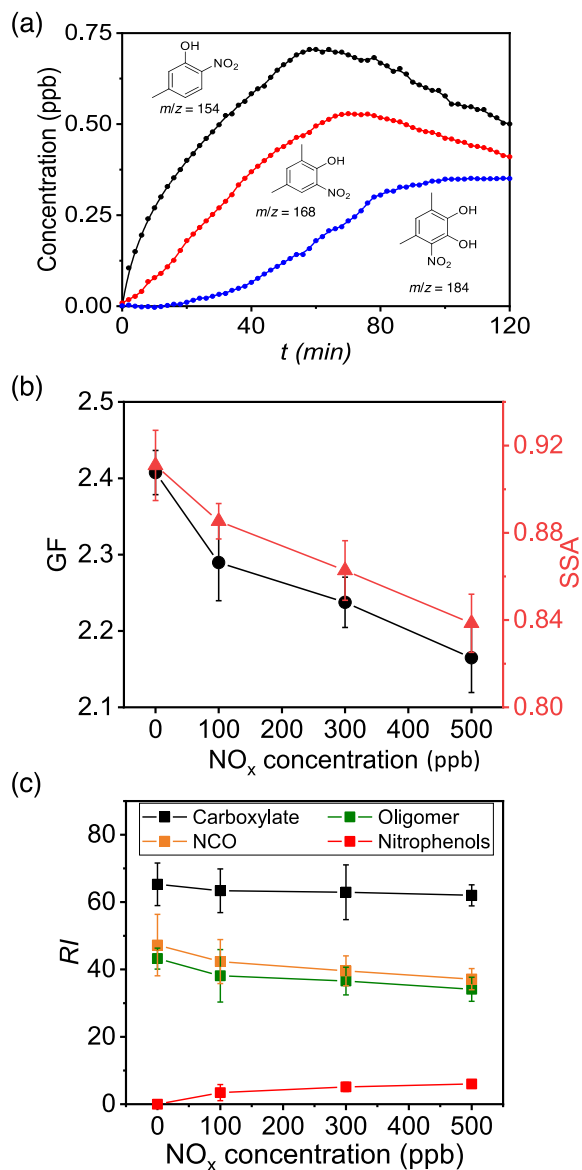
Figure 6. The effects of NO$_x$. (a) Time-dependent gas-phase concentrations of 5-methyl-2-nitrophenol (black, $m/z = 154$), dimethyl nitrophenol (red, $m/z = 168$), and dihydroxy nitrotoluene (blue, $m/z = 184$). The numbers denote the mass to charge ratio (m/z). Initiation of photooxidation by ultraviolet light occurred at $t = 0$. (b) GF (black) and SSA (red) at 120 min with varying NO$_x$ concentration from 0 to 500 ppb. (h) Dependence of aerosol-phase relative mass intensities (RI) for carboxylates (black), oligomers (green), NCO (brown), and nitrophenols (red) on NO$_x$ concentration for $(NH_4)_2SO_4$ seed particles with 19 ppb NH$_3$ at RH = 70%. The error bar denotes 1σ of 3 replicated measurements.
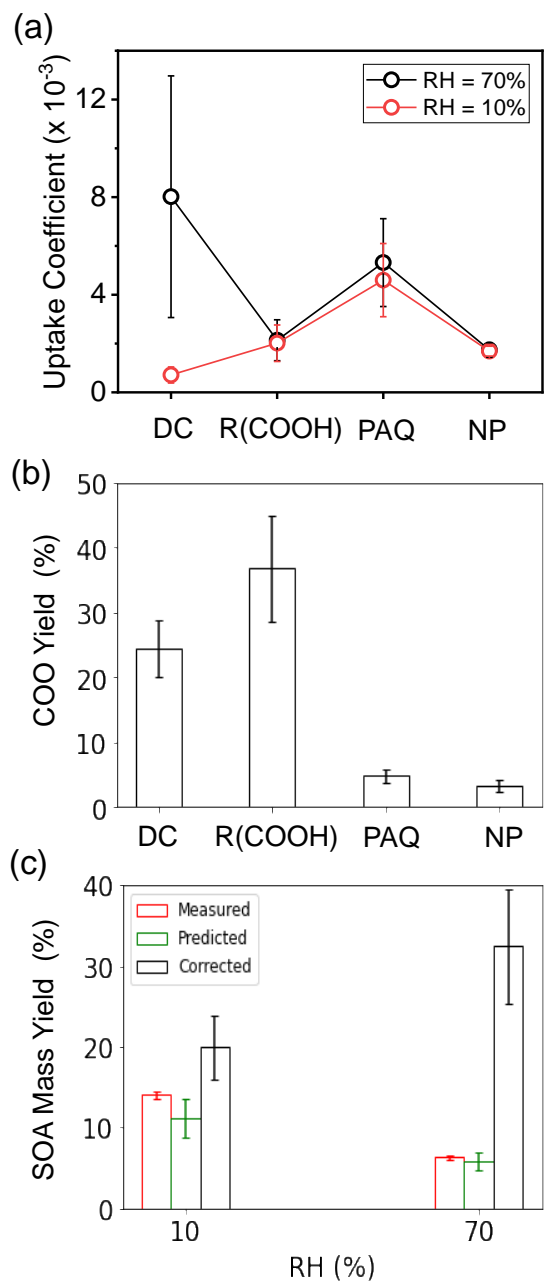
Figure 7. Uptake coefficient, COO yield, and SOA mass yield. (a) Average uptake coefficients (γ) for different types of COOs at 10% (red) and 70% (black) RH for $(NH_4)_2SO_4$ seed particles with 19 ppb NH_3 at 298 K. (b) COO yields: dicarbonyls, organic acids, polyhydroxy aromatics/quinones, and nitrophenols are represented by DC, $R(COOH)_n$, PAQ, and NP, respectively. (c) SOA mass yields at 10% (left columns) and 70% RH (right). The red, green, and black columns represent the measured, predicted, and corrected (for wall loss) SOA mass yields according to eq. 19-22. All experiments are carried out for 14 $\mu g\ m^{-3}$ $(NH_4)_2SO_4$ seed particles with 19 ppb NH_3 at 298 K. The error bars denote the 1σ of 3 replicated measurements or by accounting for error propagation of the measured parameters.

799 **Table 1. Summary of experimental conditions.**

Experiment #	Seed particle	NH_3 concentration (ppb)	NO_x concentration (ppb)	RH
Exp. 1	AS	19	0	70%
Exp. 2	AS	0	0	70%
Exp. 3	ABS	0	0	70%
Exp. 4	NaCl	0	0	70%
Exp. 5	AS	9.5	0	70%
Exp. 6	AS	28.5	0	70%
Exp. 7	ABS	9.5	0	70%
Exp. 8	ABS	19	0	70%
Exp. 9	ABS	28.5	0	70%
Exp. 10	NaCl	9.5	0	70%
Exp. 11	NaCl	19	0	70%
Exp. 12	NaCl	28.5	0	70%
Exp. 13	AS	19	0	10%
Exp. 14	AS	19	0	30%
Exp. 15	AS	19	0	50%
Exp. 16	AS	19	100	70%
Exp. 17	AS	19	300	70%
Exp. 18	AS	19	500	70%

800

801